







Extended spin coherence of the zinc-vacancy centers in ZnSe with fast optical access

Erik Kirstein ¹✉, Evgeny A. Zhukov^{1,2}, Dmitry S. Smirnov ², Vitalie Nedelea¹, Phillip Greve¹, Ina V. Kalitukha ², Viktor F. Sapega², Alexander Pawlis³, Dmitri R. Yakovlev ^{1,2}, Manfred Bayer ^{1,2} & Alex Greilich ¹✉

Qubits based on crystal defect centers have been shown to exhibit long spin coherence times, up to seconds at room temperature. However, they are typically characterized by a comparatively slow initialization timescale. Here, fluorine implantation into ZnSe epilayers is used to induce defect states that are identified as zinc vacancies. We study the carrier spin relaxation in these samples using various pump-probe measurement methods, assessing phenomena such as resonant spin amplification, polarization recovery, and spin inertia in transverse or longitudinal magnetic field. The spin dynamics in isotopically natural ZnSe show a significant influence of the nuclear spin bath. Removing this source of relaxation by using isotopic purification, we isolate the anisotropic exchange interaction as the main spin dephasing mechanism and find spin coherence times of 100 ns at room temperature, with the possibility of fast optical access on the picosecond time scales through excitonic transitions of ZnSe.

¹Experimentelle Physik 2, Technische Universität Dortmund, Dortmund, Germany. ²Ioffe Institute, Russian Academy of Sciences, St. Petersburg, Russia. ³Peter Grünberg Institute, Forschungszentrum Jülich, Jülich, Germany. ✉email: erik.kirstein@tu-dortmund.de; alex.greilich@tu-dortmund.de

Advances in quantum technology have been made rapidly in recent years, so that quantum computing, for example, no longer has remained just a dream^{1,2}, but seems to be short-term achievable^{3,4}. Steps toward practical application demand new designs which often require new systems. Nowadays, there are various quantum systems, like superconducting circuits^{1,5}, ion traps⁶, quantum dots⁷, and defect centers^{8,9}, each demonstrating promising, but also challenging features. The progress may finally lead to systems combining hybrid solutions that fulfill the requirements of specific realizations.

Two major criteria for quantum bits (qubits) are the long coherence and the efficient access¹⁰. These two requirements contradict somewhat each other, as the first one typically needs qubit isolation from the environment, while the second one requires strong coupling to it.

Several prominent solid-state implementations fulfill these criteria by using long-living, isolated qubits in a crystal structure, with optical accessibility through excitation across the optical band gap. Some of these qubits are based on defect centers, like nitrogen- or silicon-vacancies in diamond or divacancies in silicon carbide^{8,11–13}. The nitrogen-vacancies exhibit spin coherence times up to seconds at room temperature⁵, which has enabled the demonstration of quantum correction algorithms^{14,15}. On the other hand, these qubits are characterized by comparatively slow initialization in the range of hundreds of nanoseconds^{11,16}.

Resident carriers localized in self-assembled semiconductor quantum dots are alternative qubit candidates¹¹. Quantum dots show a large exciton oscillator strength which allows ultra-fast (picosecond) optical initialization and manipulation⁵. However, the spin coherence for resident carriers in quantum dots is typically limited to the microsecond range at low temperatures (around 10 K)^{17,18}.

In this study, we present a system that has a potential to offer a compromise between the two demands. We plan to take the advantage of the long spin coherence time of deep defect centers, while maintaining ultra-fast optical access for spin control, employing exciton transitions influencing the state of the resident carrier spin, similar to quantum dots.

The system of choice is defect centers in ZnSe, which have been studied for decades. Among others, we highlight initial reports of Adachi and Machi in 1977¹⁹, Dunstan et al.²⁰, and a later study of Watkins²¹ giving an insight into spectroscopy of different types of defects in ZnSe. These studies represent characteristics that distinguish defect centers of different materials from each other, like emission energy and g factors, with strong theoretical support from Laks et al.²² and dos Santos et al.²³. In recent years, the research of defect centers in ZnSe has gone out of focus, mainly due to their detrimental influence on the optical properties. It led to the result, that so far, their promising spin properties have been unexploited.

Here, we focus on one particular center, the zinc vacancy (V_{Zn}), introduced by ex-situ fluorine implantation in the crystal. First, we find that the main source of spin dephasing of zinc vacancies is the interaction with nuclear spins. Then we eliminate the non-zero nuclear spin isotopes using isotopic purification²⁴, so that the spin dephasing becomes dominated by the next available process, the anisotropic exchange interaction. In this case, we also observe long spin coherence times up to 100 ns even at room temperature and suggest strategies for its extension.

Results

Effects of implantation. Before we discuss the spin dynamics, we compare the two samples presented in Fig. 1a and demonstrate the effect of fluorine implantation on their optical properties.

The sample descriptions are given in the “Methods” section and Supplementary Note S1, here we only highlight the main differences. Both samples were taken from the same wafer with natural isotopic abundances. Reference sample A is as-grown and demonstrates the typical photoluminescence of a high-quality ZnSe epilayer (black curve), see “Methods” for details about photoluminescence measurements. The single intense peak associated with free exciton recombination (FX) is found around 2.806 eV, see Figs. 1a and b. The line at lower energy is a trace of donor-bound excitons (D^0X), caused by an unintended background doping with fluorine. We normalized the photoluminescence by the peak intensity at 2.8 eV. The doping density at the level of 10^{15} cm^{-3} was estimated from previous experiments²⁵. At lower energies, a broadband with small intensity, centered around 2.3 eV, is seen. We have multiplied this part of a spectra by an additional factor 50 to make the peak visible. It is associated with intrinsic defects incorporated during the molecular beam epitaxy growth, such as stacking faults or stoichiometric imperfections²⁶.

The red shaded curve in Fig. 1a shows the spectrum of the same sample after fluorine implantation (sample B) (normalized to the peak intensity at 2.28 eV). Instead of the expected rise of the donor-bound exciton line around 2.8 eV, which is usually associated with n -type doping by fluorine²⁵, the intensity of the defect band rises drastically. In comparison, the FX and D^0X emission is quenched almost completely. The intensity at 2.8 eV is by a factor of 82 smaller than for the sample A. This behavior is connected with the incorporation of defects in the lattice by the fluorine implantation. Zn and Se atoms can be scattered out of their initial places, leaving a vacancy, or being displaced to an interstitial site, or forming a complex with an incorporated fluorine. The most likely scenario is the creation of zinc vacancies V_{Zn} as sketched in Fig. 1c. Electronically the zinc vacancy acts as an acceptor, which is typically negatively charged in n -type materials^{21,26}. The corresponding defect centers in ZnSe have been investigated for over four decades. The interested reader can refer to refs. 20,21 for experimental studies and refs. 22,23 for defect energy calculations.

In addition, the characteristic signature of donor–acceptor pair (DAP) recombination appears in the spectrum with a photoluminescence maximum at 2.73 eV²⁷. The DAP emission demonstrates four peaks with equidistant separation of 30 meV in agreement with the LO-phonon energy²⁸.

Natural isotope composition—influence of nuclear spins. In what follows, we discuss the spin relaxation mechanisms. Figure 2a demonstrates the time-resolved Kerr rotation signal measured for sample B in the transverse magnetic field $B_{\perp} = 0.5 \text{ T}$ by degenerate pump-probe (see “Methods”), using excitation in spectral vicinity to the FX transition, see the blue curve measured at 2.8 eV and $T = 1.6 \text{ K}$. In addition, the full spectral dependence of the Kerr rotation amplitude is presented in Fig. 1b by blue dots and is described in the “Discussion” section. Two oscillating components with Lande factors of $g = 1.1$ and $g = 2$ can be extracted from this trace, both having similar amplitudes. $g = 1.1$ coincides with the g factor known from previous studies of sample A, the non-implanted version of sample B, and is related to the electron spin in the donor-bound complex (D^0X)^{25,29}. The $g = 2$ component appears only after the fluorine implantation and strongly contrasts the expected g factor of 1.1. This is a clear indication that the detected signal arises from electrons bound to the deep-centers, as in this case only a weak renormalization compared to the free electron g factor of 2 is expected³⁰. In fact, this g factor is matching the values measured for V_{Zn} ²⁰, which supports our assumption for the type of observed defects.

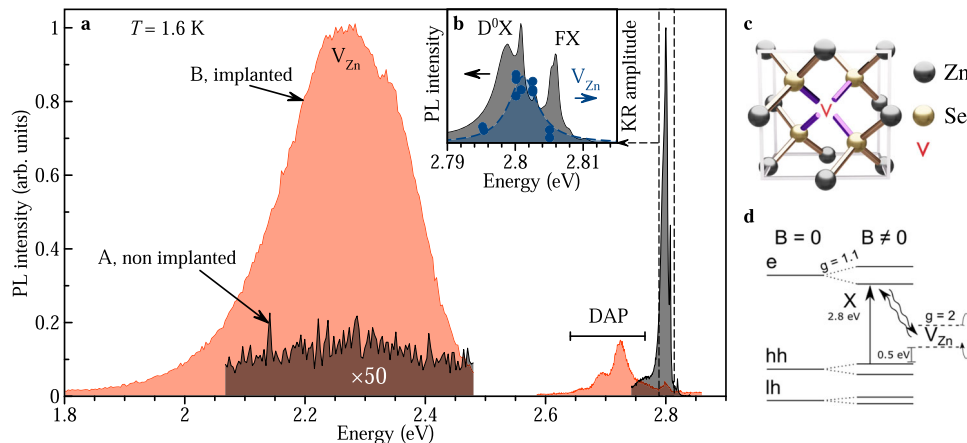


Fig. 1 Optical characterization. **a** Normalized photoluminescence (PL) of reference sample A (black curve) with pronounced emission from free exciton (FX) at 2.806 eV and donor-bound excitons (D⁰X). For the fluorine implanted sample B (red line) these emission features are quenched, but a broad band related to zinc vacancies appears around 2.3 eV. Recorded at $T = 1.6$ K. **b** Zoom of PL spectrum of sample A around 2.8 eV. High (low) energy line is associated with FX (D⁰X). Blue dots with dashed line give Kerr rotation (KR) signal amplitude of V_{Zn} vs. pump-probe energy for sample B. KR signal has maximum close to the D⁰X transitions. **c** Zinc-blende unit cell with Zn vacancy (red letter V). The vacancy is surrounded by Se atoms (yellow balls), which have further bonds to Zn-atoms (gray balls). **d** ZnSe energy level scheme. Straight arrow marks the laser excitation, curved arrows demonstrate the coupling of defect state with exciton.

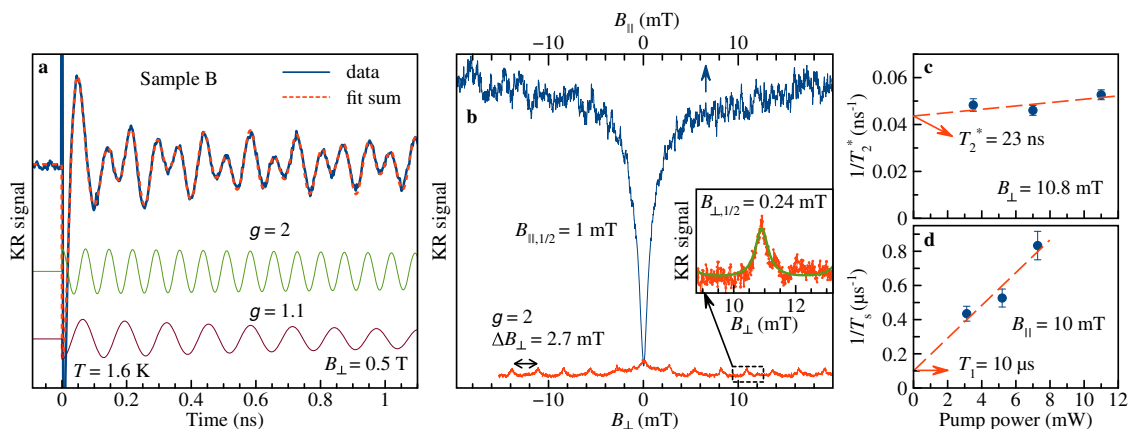


Fig. 2 Spin dynamics of V_{Zn} in the isotopically natural sample B. **a** Time-resolved Kerr rotation signal (blue), with a fit to it (red dashed). Contributing components extracted from the fit are shown below with $g = 2$ (green) and $g = 1.1$ (dark red). Spin dephasing of $g = 1.1$ component is significantly shortened compared to non-implanted sample A, see Supplementary Note S2. **b** PRC (blue) and RSA (red) curves. Half width at half maximum (HWHM) of the PRC is $B_{\parallel,1/2} = 1$ mT. Component with $g = 2$ is present in RSA. (inset) Zoom into small magnetic field range of the RSA curve, with a fit to it (green). Pump power is 3.5 mW. **c** Data points for T_2^* extracted from RSA peak width for different pump powers are shown by blue dots. Linear fit by red dashed line extrapolates to zero power and gives maximum achievable $T_2^* = 23$ ns for the $g = 2$ component. **d** Power dependence of T_1^{-1} measured by the spin inertia method. $T_1 = 10$ μs is determined by linear extrapolation to zero power. For all curves, pump and probe energies were 2.8 eV. $T = 1.6$ K. All error bars are given by the standard deviations from the fits.

As the conventional pump-probe method is restricted in the maximal measurable time span to the repetition period of the pulsed laser, in our case $T_R = 13.2$ ns, we use a modified version of it, called resonant spin amplification (RSA)^{31,32} (see “Methods” section for more details). The RSA signal with the pump energy at 2.8 eV is shown in Fig. 2b by the red curve, demonstrating a periodic peak pattern. The magnetic field separation of the observed peaks, $\Delta B = 2.7$ mT, allows us to confirm the Lande g factor of the carriers. Using the laser repetition period T_R we determine the g -factor value of 2 by $g = h/(T_R \mu_B \Delta B)$, with h being the Planck constant and μ_B the Bohr magneton.

Furthermore, the width of the measured RSA peaks gives a direct measure for the inhomogeneous spin dephasing time T_2^* . Using Eq. (1) defined in the “Methods” section we evaluate T_2^* for the $g = 2$ component, see Fig. 2b with the inset. The extrapolation to zero pump power gives $T_2^* = 23$ ns, see Fig. 2c. The half width

at half maximum (HWHM) of the RSA peaks ($B_{\perp,1/2} = 0.24$ mT) is given for illustrative and comparative purposes.

Different from sample A, where the spin component with $g = 1.1$ has a $T_2^* = 33$ ns²⁵, sample B shows $T_2^* = 2$ ns by the extrapolation to zero pump power at $B_{\perp} = 0.2$ T (not shown here), and therefore no contribution of this g -factor component to the RSA signal is expected. This indicates an acceleration of the spin dephasing to values below the laser repetition time of 13.2 ns, caused by the defect implantation in ZnSe.

In addition, we studied the electron spin polarization in dependence on the longitudinal magnetic field B_{\parallel} . The blue curve in Fig. 2b represents such a measurement, called the polarization recovery curve (PRC), see “Methods”. Typically, the dip around zero magnetic field is caused by intrinsic magnetic fields with components orthogonal to the longitudinal direction, which become overpowered by the external magnetic field, leading to

spin stabilization until saturation is reached. For localized carrier spins, the randomly oriented internal fields typically arise from the nuclear spins, and the HWHM of the observed peak $B_{\parallel,1/2}$ is directly related to the spread of these fields, the field fluctuations^{33,34}. As discussed in ref.²⁵ for sample A, the spin dephasing of the donor-bound electron with $g = 1.1$ is limited by the nuclear fluctuations of the naturally abundant isotopes in ZnSe. The same is true here for the strongly localized $g = 2$ electrons. After fluorine implantation, the zinc vacancy is surrounded by nuclear spins with natural abundance: ^{77}Se (7.58% abundance, nuclear spin $I = 1/2$) and ^{67}Zn (4.11%, $I = 5/2$), leading to the $B_{\parallel,1/2} = 1$ mT width of the PRC peak. This is a typical value for PRC curves in ZnSe. For example, sample A demonstrates $B_{\parallel,1/2} = 3.9$ mT²⁹.

To evaluate further factors limiting the spin lifetime, we have measured the longitudinal spin relaxation time T_1 employing the spin inertia method^{29,35}. Essentially, the spin amplitude of the Kerr rotation signal depends on the modulation frequency of the pump helicity. The signal decreases if repolarization by pump occurs too fast for the electron spins to reach the new equilibrium orientation, see the “Methods” section for details. Figure 2d demonstrates the dependence of the spin lifetime T_s , measured as a function of pump power. By extrapolating this time, measured for different powers, to zero power, one obtains the longitudinal spin relaxation time T_1 . At the low temperature of $T = 1.6$ K we obtained $T_1 = 10$ μs for the $g = 2$ spin component. This is about six times longer in comparison to the $T_1 = 1.6$ μs , measured for the $g = 1.1$ electrons in sample A²⁹. This might be explained by a stronger localization of the carriers at the deep vacancy centers. To simplify the comparison between both samples, we summarized measured times in Table 1. In addition, Supplementary Note S2 demonstrates the collection of similar measurements for the non-implanted sample A.

Isotopically purified sample—spin relaxation without nuclear effects. To examine the effect of the nuclear spins, we probe the zinc-vacancy carrier spin relaxation times in the structurally similar ZnSe sample C. The latter has a similar fluorine implantation dose as sample B, but the Zn and Se nuclei are isotopically purified ^{64}Zn and ^{80}Se isotopes which exhibit zero nuclear spin. More details, also on the optical properties, are given in the “Methods” section and Supplementary Notes S1 and S3.

Figure 3a demonstrates the time-resolved Kerr rotation signal of this sample, measured by degenerate pump-probe for excitation into the FX transition at 2.805 eV, see the blue curve. The trace demonstrates single-frequency oscillations corresponding to $g = 2$ with a non-decaying amplitude within the pulse separation of $T_R = 13.2$ ns. Similar to previous samples, we measure the RSA signal, which is shown in Fig. 3b by the red curve. While the measured peak distance corresponds again to the g factor of 2, the RSA peak widths are much narrower, indicating a longer spin dephasing time, e.g., $B_{\perp,1/2} = 0.014$ mT for sample C vs. 0.24 mT for sample B. Using Eq. (1) we evaluate the T_2^* as function of pump power, see Fig. 3c. The extrapolation to zero pump power gives $T_2^* = 0.4$ μs at $T = 1.6$ K which is a factor of

17 longer than $T_2^* = 23$ ns for the isotopically natural sample B, see Table 1.

Remarkably, T_2^* in sample C is only weakly affected by the temperature, see Fig. 3d. At $T = 300$ K we obtain $T_2^* \approx 0.1$ μs . We describe the temperature dependence using the Arrhenius equation, which gives the T -dependence of the spin dephasing by a term accounting for phonon activation^{28,36}: $1/T_2^*(T) = 1/T_2^*(0) + 1/T_A \exp(-E_A/k_B T)$ ³⁷. Here $T_2^*(0) = 0.4$ μs is the spin dephasing time at low temperatures, $T_A = 80$ ns the thermal relaxation coefficient, $E_A = 14$ meV the activation energy, and k_B the Boltzmann constant. In the range of $T = 1.6$ –30 K, the spin dephasing time is nearly constant. The activation energy is in agreement with the one for resident electrons in structural similar ZnSe epilayers²⁵ and in isotopically purified quantum wells³⁸. We will consider the reason for this dependence in the “Discussion” section.

In addition, we observe, that the RSA peaks width is not changing over a broad range of magnetic fields, corresponding to a vanishing spread of g factor, $\Delta g < 0.001$. This demonstrates a high homogeneity of the ground state splitting, despite the strong inhomogeneous broadening of the optical transition energies leading to the broadband of the defects photoluminescence, see Fig. 1a. A g -factor spread becomes also not noticeable with increasing temperature. The corresponding measurements are presented in Supplementary Note S4. This observation further supports the conclusion, that the signal is originating from strongly localized deep defect states, which have a high homogeneity of the g -factor values. This property demonstrates an advantage over the quantum dot systems, which are inhomogeneous in their g -factor distributions due to a variation of the material content and sizes of the quantum dots.

The inset in Fig. 3e demonstrates the dependence of the Kerr rotation amplitude as function of the pump helicity modulation frequency f_m , measured at the longitudinal magnetic field of $B_{\parallel} = 4$ mT, for the pump power of 7 mW. The drop of the amplitude at higher frequencies allows us to extract the spin lifetime T_s at a particular pump power. By extrapolating the T_s values measured at different pump powers to zero power, we extract $T_1 = 8$ μs for $T = 1.6$ K. This value is close to the one obtained in the isotopically natural sample B ($T_1 = 10$ μs). This suggests that while the vacancy spin dephasing time is strongly affected by the nuclear surrounding, the longitudinal spin relaxation is not. In addition, the $T_2^* = 0.4$ μs is about 20 times shorter than the measured T_1 , hinting at the presence of an additional mechanism limiting the spin dephasing at low temperatures, as discussed in the “Discussion” section. For convenience, we have summarized the measured times for V_{Zn} in natural and isotopically purified samples in Table 2.

Furthermore, as one can see in Fig. 3b from the red curve, the RSA signal shows a strongly reduced amplitude around zero magnetic field. For the case of sample B with naturally abundant nuclear isotopes, such a behavior can be linked with the hyperfine interaction of the localized resident carrier spins with the surrounding nuclear spins³⁴. For the sample C, however, the interaction with nuclei is strongly reduced. As discussed in ref.³⁹, the inequality of longitudinal and transverse spin relaxation times $T_1 \neq T_2$ can also lead to such a suppression of the zero RSA peak. In the studied sample T_1 is indeed much longer than the observed T_2 .

At room temperature $T_1 = 71$ ns, which becomes the limiting factor for the spin dephasing time T_2^* , see the blue dots in Fig. 3e. In the ultimate case, when the spin relaxation is only driven by the interaction with phonons, the limit of $T_2 = 2T_1$ is expected⁴⁰. Hence, the $T_2^* = 0.1$ μs comes close to the spin coherence time T_2 and the ensemble of spins acts as a macroscopically coherent magnetization.

Table 1 Spin relaxation times in samples with natural isotope composition.

	Sample A		Sample B	
	T_2^*	T_1	T_2^*	T_1
$g = 1.1$	33 ns	1.6 μs	2 ns	-
$g = 2$	-	-	23 ns	10 μs

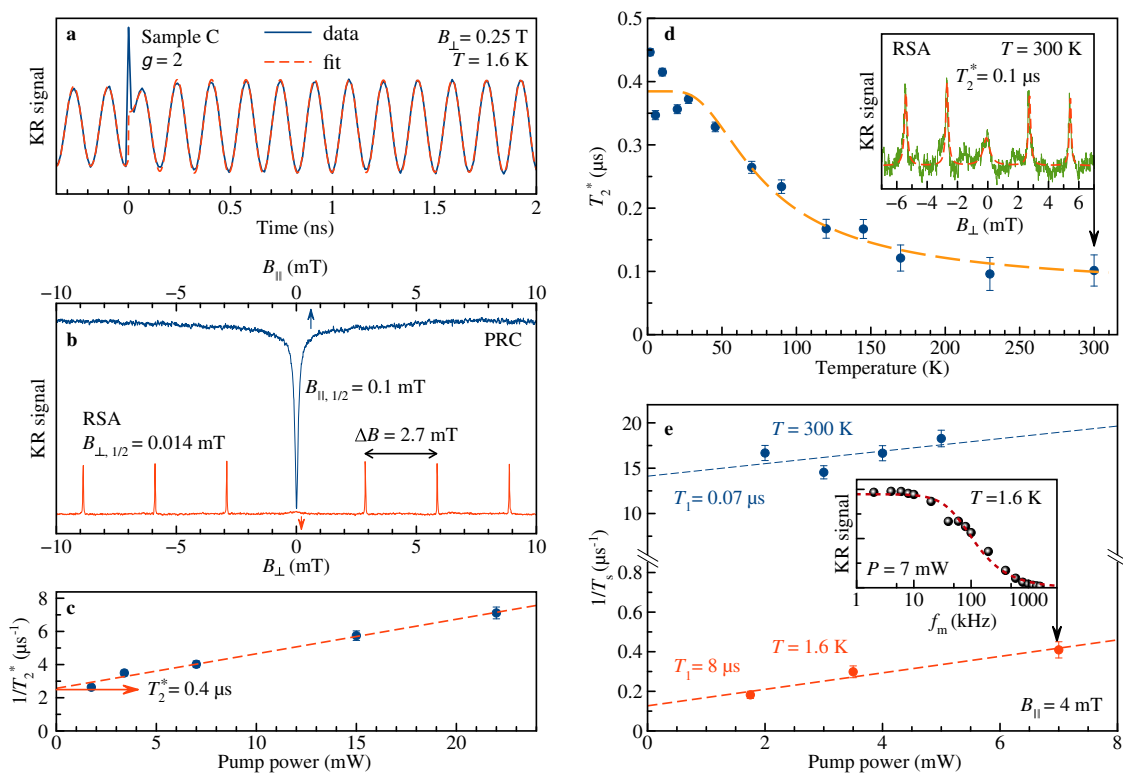


Fig. 3 Spin dynamics of V_{Zn} in isotopically pure sample C. **a** Time-resolved KR signal (blue) measured at $B_{\perp} = 0.25$ T, with a fit to it (red dashed). **b** KR signal of V_{Zn} measured at fixed time delay of -10 ps vs. magnetic field in Faraday- (PRC, blue) or Voigt- (RSA, red) direction. RSA shows very narrow peaks with separations corresponding to $g = 2$, while their width reveals $T_2^* = 0.4$ μ s. Narrow PRC dip has the HWHM of $B_{\parallel,1/2} = 0.1$ mT. **c** Data points for T_2^* extracted from RSA peak width for different pump powers are shown by blue dots, linear fit is red dashed line. Extrapolation to zero power gives maximum achievable $T_2^* = 0.4$ μ s. **d** T_2^* as function of bath temperature, with blue dots being the experimental data and red dashed line the fit by the Arrhenius equation. The laser energy was adjusted for each temperature. (inset) RSA for room temperature with data (green) and fit (red dashed line). Note, that higher temperature leads to reduced suppression of the zero RSA peak, as T_1 approaches T_2^* close to room temperature. **e** Pump-power dependence of T_1^{-1} gives T_1 at zero power. Blue color is measured at $T = 300$ K, red at $T = 1.6$ K. Dashed lines are fits. (inset) Example of signal for $T = 1.6$ K at $P = 7$ mW. KR amplitude drops as the spin polarization cannot follow the helicity modulation of excitation pulses. For $T = 1.6$ K the pump-probe energy is 2.805 eV, and for $T = 300$ K, 2.692 eV. All error bars are given by the standard deviations from the fits.

Table 2 Spin relaxation times of V_{Zn} in samples with natural and purified isotope composition at $T = 1.6$ K.

	Natural (B)	Purified (C)
T_2^* [μ s]	0.023	0.4
T_1 [μ s]	10	8

For completeness, the blue curve in Fig. 3b represents a PRC measurement in isotopically purified sample C. Compared to isotopically natural sample B, the HWHM is reduced by a factor of ten. As discussed in the previous section, the dip in the spin polarization dependence typically arises from nuclear fluctuations³⁴. This is not the case for the isotopically purified sample, so that another mechanism has to be responsible for its appearance, as will be considered in the “Discussion” section.

Discussion

In this section, we summarize the observations and consider the relevant mechanisms for spin initialization and relaxation.

In all measured structures, the spin polarization was created by excitation close to the FX and D^0X transitions. As the photoluminescence signal around these energies is quenched in the implanted samples, we measured the Kerr rotation signal amplitude by varying the photon energy of the degenerate

pump-probe pulses over the spectral range corresponding to the transition energies observed in the non-implanted samples. We discovered, that the Kerr rotation signal is only present in a narrow spectral range, but vanishes elsewhere, see the blue circles with blue shaded area in Fig. 1b for sample B and Supplementary Fig. S2 for sample C. As observed for sample B in Fig. 1a, the spectral range of the V_{Zn} emission band is about 200 meV wide. If one would excite it directly with a picosecond laser having a pulse width of about 1.5 meV it would only cover about 1% of the band, while in contrast, the 6–10 meV-broad spectral range of strong Kerr rotation amplitude is covered well by the picosecond laser and leads to efficient excitation.

After excitation in the FX range, the optically created excitons are efficiently captured by V_{Zn} , initializing the spin polarization in the deep defect centers. This is supported by measurements in Supplementary Note S5, demonstrating a circular polarization of the photoluminescence from the defect states after optical FX excitation. Furthermore, Supplementary Note S6 shows the time-resolved photoluminescence of the defect band with the signal rise-time of about 200 ps, which is at the lower limit of the experiment’s time resolution. This capture process leads to the photoluminescence quench of FX and D^0X and the rise of the photoluminescence from the defect band, as seen in the photoluminescence spectrum in Fig. 1a. See also Supplementary Notes S7–S11 for supporting measurements on the initialization and identification of the V_{Zn} centers.

The fact, that the Kerr rotation signal can be measured at energies close to the FX transition and does not originate from the state optically addressed directly, is well known for Kerr studies and can be seen analogous to excitation and readout of D⁰X centers that are shifted from the band gap energy by the exciton binding energy^{41,42}.

The optical initialization and the Kerr rotation are related to the exchange interaction of the vacancies with the excitons, as shown in Fig. 1d. In particular, the exchange interaction between spin-polarized vacancies and virtual excitons generates the Kerr rotation signal due to shifting and broadening of the exciton optical transition⁴³.

This excitation scheme also explains the observed temperature dependence in Fig. 3d. As the Kerr rotation signal is produced through the exchange interaction of deep-center spins with electrons around the FX or D⁰X transitions, the thermal delocalization of these electrons leads to the signal reduction from the deep-centers.

In Table 3 we present the summary of spin relaxation times for the $g = 2$ component in the time-resolved Kerr rotation signals from the measured samples.

Considering the discussed samples, we can draw conclusions about the relevant spin relaxation mechanisms. As determined from the RSA and PRC dependencies in refs. 25,29, the spin dephasing of the donor-bounded electrons with $g = 1.1$ in sample A is related to the hyperfine interaction. After fluorine implantation (sample B), the spin dephasing of the $g = 1.1$ component is accelerated. Here, also the second component with $g = 2$ appears, which we relate to the deep vacancy states. These demonstrate longer T_1 and similar T_2^* , compared to the donor-bounded states. Also here, we relate the observed spin dephasing to the interaction with non-zero nuclear spins. In the next step, we removed the non-zero nuclear spins by isotopic purification. The observed PRC width is strongly reduced, but is, however, still present, see the blue curve in Fig. 3b.

One possibility to explain the presence of the PRC dip would be a weak residual hyperfine interaction with the remote nuclei even for strongly localized electrons. If we consider the more abundant selenium atoms (Se⁷⁷), that also have one order of magnitude higher hyperfine constant than zinc²⁵, we can estimate a reduction factor of about 7.58% (Se⁷⁷)/(100% – 99.997% (Se⁸⁰)) = 2527 for non-zero Se⁷⁷ spins after a purification. Since T_2^* is inversely proportional to the square root of the abundance of non-zero nuclear spins³³, this, in principle, deviate by a factor of 3 from our measurements of 400 ns, with $T_2^* = 23\sqrt{2527}$ ns = 1156 ns. Although it does not contradict our observations completely, we consider further possible mechanisms.

Another possibility to explain the presence of the PRC dip is strain in the structure^{25,44}. However, the singly negatively charged zinc vacancies have C_{3v} point symmetry due to the Jahn-Teller distortion⁴⁵. All the irreducible spinor representations of this group are twofold degenerate, so a vacancy can be characterized by a pseudo-spin 1/2. Noteworthy, the two corresponding states cannot be split in zero magnetic field because of the Kramers degeneracy despite of the strong strain effects.

Taking further into account that the spin dephasing is weakly dependent on magnetic field ($\Delta g \approx 0$) and no interaction with

nuclear spins is present, the anisotropic exchange interaction (Dzyaloshinskii-Moriya, DMI) can be considered as the main source of spin dephasing in isotopically purified samples^{46,47}. In the Supplementary Note S12, we show that the observed polarization recovery and Hanle effect can be explained by the DMI in small clusters of vacancies for the isotopically purified samples.

Conclusion. To conclude, we have demonstrated that zinc-vacancy centers in an isotopically purified ZnSe host lattice show an ensemble coherence in the sub-microsecond range, ultra-fast spin initialization, and an efficient readout via the exciton transition of the ZnSe host material. The spin coherence time remains long up to room temperature at about 0.1 μ s.

The examination of the relevant longitudinal spin relaxation and dephasing mechanisms shows a clear path for further improvement. Isotopic purification with a low density of defects should strongly extend the spin dephasing time by removing both the hyperfine and Dzyaloshinskii-Moriya interactions.

In addition, possible effects of the nuclear spin of the implanted fluorine $I = 1/2$ with 100% abundance could be removed by introducing V_{Zn} by electron irradiation^{21,27}.

Methods

Samples. We study molecular beam epitaxy (MBE) grown samples, either with natural or with isotopically purified isotope composition. For the isotopically pure samples, the grade of isotope purification of ⁶⁴Zn and ⁸⁰Se is about 99.985% and 99.997%, respectively. Details on the MBE growth and further details about the isotopically pure samples are presented in ref. 24. The epilayers are similar in respect to their structure: a 15 nm ZnSe buffer layer is grown on a (100)-oriented GaAs substrate, followed by an 18 nm Zn_{0.86}Mg_{0.14}Se barrier. On top of the barrier ≈ 70 -nm-thick ZnSe epilayer is grown. The buffer layer releases stress due to lattice mismatch, while the barrier layer prevents carrier drain into the substrate.

The Zn_{0.86}Mg_{0.14}Se barrier has a band gap of 2.88 eV⁴⁸, while the exciton energy in ZnSe is 2.806 eV at cryogenic temperatures. The sample orientation is (001) with respect to the light incidence wavevector \mathbf{k} . After MBE growth, the samples were ion implanted with fluorine using an acceleration voltage of 45 kV and an ion dose of 10^{15} cm⁻². The decelerating fluorine atoms take a random walk through the sample, scattering lattice atoms out of their positions. During implantation, the sample was kept at a temperature of 250 °C. The implantation angle of incidence was 7°.

Due to the used ion dose and the corresponding implantation time, we estimate that $\approx 1 \times 10^{18}$ cm⁻³ fluorine atoms are implanted into the sample. However, this does not provide any information about how many V_{Zn} are generated during the implantation. What is certain, however, is that an implanted fluorine atom, when it collides with a Zn or Se atoms on a lattice site, generates a whole series of sequential V_{Zn}, V_{Se}, or other point defects. We use a theoretical model based on the DMI model presented in Supplementary Note S12 to estimate the V_{Zn} concentrations to be about 10^{18} cm⁻³.

For the presented studies we used the following samples: sample A is non-purified and non-implanted, sample B is the fluorine implanted sample A, and sample C is isotopically purified and fluorine implanted using the same acceleration voltage and ion dose as for sample B.

Optical setup. The samples were placed in an optical cryostat with temperatures variable from 1.6 K up to 300 K. For $T = 1.6$ K, the sample was immersed in superfluid helium, while for 4.2–300 K the sample was held in cooling helium gas. Two types of cryostats were used. Both cryostats can generate magnetic fields through split pair coils. The first can generate magnetic fields up to 8 T along a fixed direction with a single pair coil, while the second is equipped with three split coils pair capable to apply magnetic fields up to 3 T at any solid angle. Magnetic fields parallel to \mathbf{k} are labeled B_{||} (Faraday geometry), magnetic fields perpendicular to \mathbf{k} as B_⊥ (Voigt geometry). For all measurements, we use a free beam configuration.

Photoluminescence. For measurements of the photoluminescence, the sample was excited by a diode laser at a wavelength of 405 nm with a power of 0.5 mW. The emitted light was dispersed by a 0.5 m monochromator with 1800 groves/mm grating with attached Peltier-cooled charge-coupled-device (CCD) camera.

Pump-probe time-resolved Kerr rotation. The spin dynamics are measured by a degenerated pump-probe technique⁴⁹. A Titan-Sapphire (Ti:Sa) laser generates pulses of 1.2 ps duration, in the spectral range of 700–980 nm with a spectral width of about 1 nm and a pulse repetition rate of 76 MHz (repetition period $T_R = 13.2$ ns). The light is frequency doubled by a β -Barium borate (BBO) crystal. The

Table 3 Spin relaxation times of V_{Zn} in ZnSe epilayer.

	T [K]	Natural (B)	Purified (C)
T_2^* [μ s]	1.6	0.023	0.4
	300	-	0.1
T_1 [μ s]	1.6	10	8
	300	-	0.07

laser emission is split into the pump and probe beams, with one beam delayed with respect to the other by a mechanical delay line. The pump beam is helicity modulated by an electro-optic modulator, alternating between σ^+ and σ^- at the frequency f_m in the range of 1 kHz up to 3 MHz. The probe beam is not modulated and linearly polarized. The Kerr rotation of the polarization plane of the reflected probe beam is analyzed by a Wollaston prism and balanced photo-diodes using a lock-in technique. The signal can be described with a decaying oscillatory function: $A_{KR} = S_e \cos(\omega_L t) \exp(-t/T_2^*)$, with $\omega_L = g\mu_B B/\hbar$ being the Larmor frequency.

Resonant spin amplification. In the case of T_2^* exceeding T_R the Kerr rotation signal is given not only by the signal induced by a pump, while the signals from previous pumps have disappeared, but the signals superimpose and consequently interfere^{31,32}. Depending on the ratio of precession to repetition period, either constructive or destructive interference can occur. In the constructive case, the phase synchronization condition (PSC) is met, where the Larmor frequency ω_L is tuned by the magnetic field such, that the precession period is a fraction of the pulse separation. This leads to an increase of the Kerr rotation signal, called resonant spin amplification (RSA). The shape of the RSA signal is described by

$$A_{RSA}(\omega_L, t) = \frac{S_0}{2} \exp(-t/T_2^*) \times \frac{\exp(-T_R/T_2^*) \cos(\omega_L t) - \cos[\omega_L(t + T_R)]}{\cosh(T_R/T_2^*) - \cos(\omega_L T_R)}, \quad (1)$$

where S_0 is the initial spin polarization. For the measurement, typically a short negative time delay $t = -10$ ps is chosen and the magnetic field is swept to find the PSC fields. The RSA trace then consists of a series of Lorentz-like peaks, with the width proportional to $1/T_2^*$ and the repetition period proportional to the g factor.

Spin inertia. The polarization process depends on the longitudinal relaxation time of the spins T_1 . For long T_1 a high number of pulses is needed to achieve full equilibrium polarization. If the polarization modulation frequency f_m becomes higher than $1/T_1$, equilibrium can no longer be reached. The achievable polarization is lower than in the case of low-frequency modulation:

$$A_{SI} = \frac{2|S_0|n_0}{\pi\sqrt{1 + (2\pi f_m T_1)^2}}, \quad (2)$$

with A_{SI} the obtained signal amplitude, S_0 the initial spin polarization, and n_0 the spin concentration^{35,50}. A higher excitation power, P_{pu} , leads to a smaller number of pulses required to achieve equilibrium condition, as if the lifetime would be shorter. One can show that $1/T_s(P_{pu}) = 1/T_1 + S_G P_{pu}$, with T_s being the spin lifetime limited by the generation of new spin-polarized carriers, T_1 being the longitudinal spin relaxation time, and S_G being the spin generation coefficient.

Data availability

The data on which the plots within this paper are based and other findings of this study are available from the corresponding author upon justified request.

Received: 18 May 2021; Accepted: 17 August 2021;

Published online: 06 September 2021

References

- Arute, F. et al. Quantum supremacy using a programmable superconducting processor. *Nature* **574**, 505–510 (2019).
- Stoneham, M. Trend: is a room-temperature, solid-state quantum computer mere fantasy? *Physics* **2**, 34 (2009).
- Zhong, H.-S. et al. Quantum computational advantage using photons. *Science* **370**, 1460–1463 (2020).
- Cho, A. IBM promises 1000-qubit quantum computer—a milestone—by 2023. *Science* <https://doi.org/10.1126/science.abe8122> (2020).
- Atatüre, M., Englund, D., Vamivakas, N., Lee, S.-Y. & Wrachtrup, J. Material platforms for spin-based photonic quantum technologies. *Nat. Rev. Mater.* **3**, 38–51 (2018).
- Georgescu, I. Trapped ion quantum computing turns 25. *Nat. Rev. Phys.* **2**, 278–278 (2020).
- Kloeffel, C. & Loss, D. Prospects for spin-based quantum computing in quantum dots. *Ann. Rev. Condens. Matter Phys.* **4**, 51–81 (2013).
- Weber, J. R. et al. Quantum computing with defects. *Proc. Natl Acad. Sci. USA* **107**, 8513–8518 (2010).
- Wrachtrup, J. Defect center room-temperature quantum processors. *Proc. Natl Acad. Sci. USA* **107**, 9479–9480 (2010).
- Loss, D. & DiVincenzo, D. P. Quantum computation with quantum dots. *Phys. Rev. A* **57**, 120–126 (1998).
- Ladd, T. D. et al. Quantum computers. *Nature* **464**, 45–53 (2010).
- Koehl, W. F., Buckley, B. B., Heremans, F. J., Calusine, G. & Awschalom, D. D. Room temperature coherent control of defect spin qubits in silicon carbide. *Nature* **479**, 84–87 (2011).
- Seo, H. et al. Quantum decoherence dynamics of divacancy spins in silicon carbide. *Nat. Commun.* **7**, 12935 (2016).
- Waldherr, G. et al. Quantum error correction in a solid-state hybrid spin register. *Nature* **506**, 204–207 (2014).
- Taminiau, T. H., Cramer, J., van der Sar, T., Dobrovitski, V. V. & Hanson, R. Universal control and error correction in multi-qubit spin registers in diamond. *Nat. Nanotechnol.* **9**, 171–176 (2014).
- Hopper, D. A., Shulevitz, H. J. & Bassett, L. C. Spin readout techniques of the nitrogen-vacancy center in diamond. *Micromachines* **9**, 437 (2018).
- Greilich, A. et al. Mode locking of electron spin coherences in singly charged quantum dots. *Science* **313**, 341–345 (2006).
- Press, D. et al. Ultrafast optical spin echo in a single quantum dot. *Nat. Photon.* **4**, 367–370 (2010).
- Adachi, S. & Machi, Y. Boron- and fluorine-ion-implantation into ZnSe single crystals. *Jpn. J. Appl. Phys.* **17**, 135 (1978).
- Dunstan, D. J., Nicholls, J. E., Cavenett, B. C. & Davies, J. J. Zinc vacancy-associated defects and donor-acceptor recombination in ZnSe. *J. Phys. C: Solid State Phys.* **13**, 6409 (1980).
- Watkins, G. D. Intrinsic defects in II-VI semiconductors. *J. Cryst. Growth* **159**, 338–344 (1996).
- Laks, D. B., Van de Walle, C. G., Neumark, G. F., Blöchl, P. E. & Pantelides, S. T. Native defects and self-compensation in ZnSe. *Phys. Rev. B* **45**, 10965–10978 (1992).
- dos Santos, L. S., Schmidt, W. G. & Rauls, E. Group-VII point defects in ZnSe. *Phys. Rev. B* **84**, 115201 (2011).
- Pawlis, A. et al. MBE growth and optical properties of isotopically purified ZnSe heterostructures. *ACS Appl. Electron. Mater.* **1**, 44–50 (2019).
- Greilich, A. et al. Spin dephasing of fluorine-bound electrons in ZnSe. *Phys. Rev. B* **85**, 121303 (2012).
- Watkins, G. D. In *Handbook of Semiconductor Technology Set* 121–165 (John Wiley & Sons, Ltd, 2000).
- Gutowski, J., Presser, N. & Kudlek, G. Optical properties of ZnSe epilayers and films. *Phys. Status Solidi A* **120**, 11–59 (1990).
- Tews, H., Neu, G. & De-Sheng, J. Phonon scattering at impurity pairs in ZnSe. *Phys. Rev. B* **24**, 7321–7328 (1981).
- Heisterkamp, F. et al. Longitudinal and transverse spin dynamics of donor-bound electrons in fluorine-doped ZnSe: spin inertia versus Hanle effect. *Phys. Rev. B* **91**, 235432 (2015).
- Ivchenko, E. L., Kalevich, V. K., Shiryaev, A. Y., Afanasiev, M. M. & Masumoto, Y. Optical orientation and spin-dependent recombination in GaAsN alloys under continuous-wave pumping. *J. Phys. Condens. Matter* **22**, 465804 (2010).
- Kikkawa, J. M. & Awschalom, D. D. Resonant spin amplification in n -type GaAs. *Phys. Rev. Lett.* **80**, 4313–4316 (1998).
- Yugova, I. A., Glazov, M. M., Yakovlev, D. R., Sokolova, A. A. & Bayer, M. Coherent spin dynamics of electrons and holes in semiconductor quantum wells and quantum dots under periodical optical excitation: resonant spin amplification versus spin mode locking. *Phys. Rev. B* **85**, 125304 (2012).
- Merkulov, I. A., Efros, A. L. & Rosen, M. Electron spin relaxation by nuclei in semiconductor quantum dots. *Phys. Rev. B* **65**, 205309 (2002).
- Smirnov, D. S. et al. Spin polarization recovery and Hanle effect for charge carriers interacting with nuclear spins in semiconductors. *Phys. Rev. B* **102**, 235413 (2020).
- Smirnov, D. S. et al. Theory of spin inertia in singly charged quantum dots. *Phys. Rev. B* **98**, 125306 (2018).
- Crane, M. J. et al. Coherent spin precession and lifetime-limited spin dephasing in CsPbBr₃ Perovskite nanocrystals. *Nano Lett.* **20**, 8626–8633 (2020).
- McNaught, A. D. & Wilkinson, A. (eds). *IUPAC. Compendium of Chemical Terminology*, 2nd edn (the “Gold Book”) (Blackwell Scientific Publications, 1997).
- Kopteva, N. E. et al. Spin dephasing of electrons and holes in isotopically purified ZnSe/(Zn,Mg)Se quantum wells. *Phys. Rev. B* **100**, 205415 (2019).
- Glazov, M. M. & Ivchenko, E. L. Resonant spin amplification in nanostructures with anisotropic spin relaxation and spread of the electronic g factor. *Semiconductors* **42**, 951–957 (2008).
- Golovach, V. N., Khaetskii, A. & Loss, D. Phonon-induced decay of the electron spin in quantum dots. *Phys. Rev. Lett.* **93**, 016601 (2004).
- Glazov, M. M. Coherent spin dynamics of electrons and excitons in nanostructures (a review). *Phys. Solid State* **54**, 1–27 (2012).
- Gaj, J. A. & Kossut, J. (eds). *Introduction to the Physics of Diluted Magnetic Semiconductors*. Springer Series in Materials Science (Springer-Verlag, 2010).
- Astakhov, G. V. et al. Oscillator strength of trion states in ZnSe-based quantum wells. *Phys. Rev. B* **62**, 10345–10352 (2000).
- Thomas, R. J. et al. Temperature dependence of strain in ZnSe(epilayer)/GaAs(epilayer). *J. Appl. Phys.* **78**, 6569–6573 (1995).

45. Jeon, D. Y., Gislason, H. P. & Watkins, G. D. Optical detection of magnetic resonance of the zinc vacancy in ZnSe via magnetic circular dichroism. *Phys. Rev. B* **48**, 7872–7883 (1993).
46. Kavokin, K. V. Anisotropic exchange interaction of localized conduction-band electrons in semiconductors. *Phys. Rev. B* **64**, 075305 (2001).
47. Kavokin, K. V. Spin relaxation of localized electrons in n-type semiconductors. *Semicond. Sci. Technol.* **23**, 114009 (2008).
48. Sohel, M., Muñoz, M. & Tamargo, M. C. Molecular beam epitaxial growth and characterization of zinc-blende ZnMgSe on InP (001). *Appl. Phys. Lett.* **85**, 2794–2796 (2004).
49. Dyakonov, M. I. (ed.) *Spin Physics in Semiconductors*, 2nd edn (Springer International Publishing AG, 2017).
50. Heisterkamp, F. et al. Inhomogeneous nuclear spin polarization induced by helicity-modulated optical excitation of fluorine-bound electron spins in ZnSe. *Phys. Rev. B* **92**, 245441 (2015).

Acknowledgements

We thank M.M. Glazov for fruitful discussions. We acknowledge the financial support by the Deutsche Forschungsgemeinschaft in the frame of the International Collaborative Research Center TRR 160 (Project A1). D.S.S. acknowledges the financial support by the Russian Science Foundation Grant No. 19-12-00051.

Author contributions

E.K., E.A.Z., and A.G. conceived the experiment. E.K., E.A.Z., V.N., and P.G. carried out the experiment and took the experimental data. E.K., I.V.K., and V.F.S. conceived the spin-flip Raman measurements. E.K., E.A.Z., and A.G. analyzed the experimental data. D.S.S. conceived the theoretical model. A.P. prepared the samples. E.K., D.R.Y., M.B., and A.G. wrote the manuscript.

Funding

Open Access funding enabled and organized by Projekt DEAL.

Competing interests

The authors declare no competing interests.

Additional information

Supplementary information The online version contains supplementary material available at <https://doi.org/10.1038/s43246-021-00198-z>.

Correspondence and requests for materials should be addressed to E.K. or A.G.

Peer review information *Communications Materials* thanks Louis Gaudreau and the other, anonymous, reviewer(s) for their contribution to the peer review of this work. Primary Handling Editors: Klaas-Jan Tielrooij and Aldo Isidori. Peer reviewer reports are available.

Reprints and permission information is available at <http://www.nature.com/reprints>

Publisher's note Springer Nature remains neutral with regard to jurisdictional claims in published maps and institutional affiliations.



Open Access This article is licensed under a Creative Commons Attribution 4.0 International License, which permits use, sharing, adaptation, distribution and reproduction in any medium or format, as long as you give appropriate credit to the original author(s) and the source, provide a link to the Creative Commons license, and indicate if changes were made. The images or other third party material in this article are included in the article's Creative Commons license, unless indicated otherwise in a credit line to the material. If material is not included in the article's Creative Commons license and your intended use is not permitted by statutory regulation or exceeds the permitted use, you will need to obtain permission directly from the copyright holder. To view a copy of this license, visit <http://creativecommons.org/licenses/by/4.0/>.

© The Author(s) 2021